

Article

Dynamic Polarization Behaviors of Equimolar CoCrFeNi High-Entropy Alloy Compared with 304 Stainless Steel in 0.5 M H₂SO₄ Aerated Aqueous Solution

Chao-Chun Yen¹, Ting-Lun Tsai¹, Bo-Wei Wu¹, Yu-Chieh Lo², Ming-Hung Tsai¹ and Shioh-Kang Yen^{1,*}¹ Department of Materials Science and Engineering, National Chung Hsing University, Taichung 40227, Taiwan² Department of Materials Science and Engineering, National Yang Ming Chiao Tung University, Hsinchu 30010, Taiwan

* Correspondence: skyen@dragon.nchu.edu.tw

Abstract: Three corrosion potentials and three corrosion current densities are clearly identified before the passivation for both dynamic polarization curves of equimolar CoCrFeNi high-entropy alloy (HEA) and 304 stainless steel (304SS) in 0.5 M H₂SO₄ aerated aqueous solution, by decomposing anodic and cathodic polarization curves. The passivated current density of the former is greater than the latter, compliant with not only the constant of solubility product (k_{sp}) and redox equilibrium potential (E_{eq}) of each metal hydroxide but also the sequence of bond energy (E_b) for monolayer hydroxide on their facets derived from the first principle founded on density function theory. However, the total amount of ion releasing from HEA is less than 304SS, since the hydroxide/oxide film formed in the air of the latter containing greater amounts of Fe(II) and Mn(II) is less stable around corrosion potentials while they are further oxidized into more stable Fe(III) and Mn(III or IV) with much lower k_{sp} , leading to the much less increasing ratios of ion releases from 0.25 to 0.6 V.

Keywords: high-entropy alloy; first-principles calculations; polarization; ICP-MS; passive film



Citation: Yen, C.-C.; Tsai, T.-L.; Wu, B.-W.; Lo, Y.-C.; Tsai, M.-H.; Yen, S.-K. Dynamic Polarization Behaviors of Equimolar CoCrFeNi High-Entropy Alloy Compared with 304 Stainless Steel in 0.5 M H₂SO₄ Aerated Aqueous Solution. *Materials* **2022**, *15*, 6976. <https://doi.org/10.3390/ma15196976>

Academic Editor: Sergey V. Zherebtsov

Received: 2 September 2022

Accepted: 4 October 2022

Published: 8 October 2022

Publisher's Note: MDPI stays neutral with regard to jurisdictional claims in published maps and institutional affiliations.



Copyright: © 2022 by the authors. Licensee MDPI, Basel, Switzerland. This article is an open access article distributed under the terms and conditions of the Creative Commons Attribution (CC BY) license (<https://creativecommons.org/licenses/by/4.0/>).

1. Introduction

High-entropy alloys (HEAs), unlike traditional single-element base ideas, were originally proposed as alloys composed of several major elements in equimolar or near-equal molar proportions [1,2]. By using this new concept of alloy design, the formation of intermetallic compounds can be curbed to urge the solid-solution phase(s) in the form of simple crystal structures including face-centered cubic (FCC), body-centered cubic (BCC), or hexagonal closed-pack (HCP) [3–5]. The concentrated solid-solution structures of HEAs often exhibit remarkable properties, including exceptional strength [6,7], high fatigue resistance [8], high thermal stability [9], superior electrical resistivity [10], and outstanding wear resistance [11]. However, most of the metal elements composing HEAs are thermodynamically unstable in the natural environment on the earth. Therefore, it is an important issue to design the HEAs for forming protective films to hinder or retard the environmental surrounding attacks.

It is well known that the nature of the passivation film consisting of a Cr-enriched oxide and/or hydroxide film determines the corrosion resistance of the stainless steel. King and Uhlig reported the polarization data by the adsorbed oxygen film composing the passivation film [12]. Aronowitz and Hackerman also consider it to be an absorbed single layer of oxygen [13]. The thickness of Fe–Cr alloy passivation film formed in the acidic solution ranging from 1.2–2.5 nm was analyzed by series techniques [14–21], including that Cr³⁺ oxide or hydroxide with a relatively small amount of Fe²⁺ is the major component on the film formed at a lower potential. Recently, E. Hamada reported that the thickness of passivation film formed on commercial 304 stainless steel after being kept in the atmosphere for a decade is from 3 to 5 nm [22]. Additionally, it has been shown that the adsorption of

hydroxide ions on pure metals (copper, nickel, and chromium) and chromium-containing alloys (stainless steel) precedes the growth of three-dimensional oxides and produces a two-dimensional adsorbed hydroxyl covering layer acting as the structural precursor for the growth of three-dimensional passivation film [23].

Like stainless steel, most HEAs contain passivating elements that help form passivation layers, such as Al, Cr, Mo, and the like. The corrosion behavior of CoCrFeNi-based HEA has been much revealed [24–29]. Adding different elements in equimolar CoCrFeNi-X (X = Al, Cu, Sn) causes different corrosion resistance in a chlorine environment due to the various qualities of extensive metal oxides and galvanic corrosion between phases [24]. In 0.1 M H₂SO₄, the corrosion behavior of the equimolar CoCrFeMnNi HEA was compared to 304 stainless steel (304SS) because both single FCC phase metals have similar corrosion-resistance elements. The corrosion resistance of the HEA is worse than 304SS since the passivation film of HEA was formed by various elements and meanwhile the insufficient content of Cr [29]. In the latest three years, the corrosion mechanism of tri-phase equimolar AlCoCrFeNi high-entropy alloy has been reasonably explained by combining metal hydroxides reduction-oxidation potential derived by the Nernstian equation, the solubility product constant (k_{sp}), and the compositional difference in three phases [28]. It has been reported that decreasing Ni content with increasing Fe or Co content in a single FCC phase Co_aCrFe_bNi_{80-a-b} system could reduce passivation current density and lead to improving corrosion resistance [30], while the inverse effect of Ni was found on the corrosion resistance of TiZrHfBeCu (Ni) high-entropy bulk metallic glass in 3.5 wt.% NaCl [31]. Furthermore, tuning minor additions of Ti and Al to form (CoCrFeNi)₉₄Ti_{1.5}Al_{4.5} HEA has enhanced the corrosion resistance in 0.5M H₂SO₄ for the coating on Q235 steel substrate by plasma cladding [32]. Obviously, it is an important issue for upgrading the resistant performance of HEA against the corrosive environment. However, the corrosion behavior of equimolar CoCrFeNi HEA is rarely obtained, especially for the role of each element at various potentials during the polarization and passivation.

In this study, the potentiodynamic curves of 304SS and CoCrFeNi HEA in 0.5 M H₂SO₄ aerated aqueous solutions are quite similar. The alloy equilibrium potential (E_{eg}) is calculated by the Nernst equation and Gibbs energy of individual metal, and the potentiodynamic curves are decomposed into anodic curves and cathodic curves to understand the reaction at each potential precisely. According to density function theory (DFT), the first-principles calculations have been used to design a new organic inhibitor for corrosion [33] or to investigate the adsorption of oxygen on metal surfaces [34,35]. In addition, it was also applied to assess the stability (the dissipated energy) of monolayer hydroxide on the tri-phase HEA [28]. Consequently, such a calculation conducted for the CoCrFeNi HEA and 304SS may also play a crucial role in the corrosion performance.

2. Materials and Methods

2.1. Sample Preparation

The CoCrFeNi HEA was manufactured by using Co, Cr, Fe, and Ni metal grains with high purity (99.99 wt%) according to molar ratios as primary materials and then placed in the inner side of a water-chilled Cu crucible and melted by arc in Ar atmosphere. The melting solidification process was repeated for three cycles to ensure the liquid homogenized completely, and then cooled to ambient temperature for deriving the as-cast ingot. The chemical compositions of CoCrFeNi HEA and commercial 304SS traded from the market characterized by energy dispersive spectroscopy (EDS) analysis are listed in Table 1, where elements such as C 0.06%, P 0.045% and S 0.015% less than 1% are neglected.

Table 1. Compositions of CoCrFeNi HEA and 304SS by EDS analyses (at. %).

Elements	Co	Cr	Fe	Ni	Mn	Si
304SS	-	20.65	68.65	7.50	2.12	1.08
CoCrFeNi HEA	24.36	26.85	25.18	23.61	-	-

Test specimens were made by the wire cutting during electrical discharge then spot-welded with copper lines on the back side for the electrical conduction and finally cold-mounted in epoxy. The front side with exposed surface area 0.25 cm^2 was wet ground by SiC papers ranging from grit number 100 to 2000, polished with alumina powder sized from 1 to $0.3 \mu\text{m}$ and cleaned thoroughly in a deionized water bath with an ultrasonic generator before each kind of electrochemical measurement.

2.2. Electrochemical Measurements

The electrochemical tests were carried out in a three-electrode cell. The working electrode was the specimen with surface area 0.25 cm^2 immersed in $0.5 \text{ M H}_2\text{SO}_4$ aerated aqueous solution (AAS) at ambient temperature, using a commercial Ag/AgCl electrode in saturated KCl solution as the reference electrode (Ref) and a Pt plate was the auxiliary electrode. The potentiodynamic polarization measurement was conducted at scan rate 0.167 mV/s from initial potential -1.2 V to final potential 1.2 V versus the open current potential (OCP) (vs. E_{ocp}) by Multi Potentiostat VSP and EC-lab software 11.35 (Bio-logic, Seyssinet-Pariset, France). Furthermore, the samples were kept at a constant potential of 0.6 V (vs. Ref) for 2 h to record the variation of current density for both metals.

2.3. Component Analyses of the Passivation Films

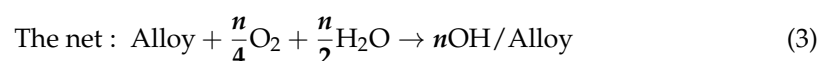
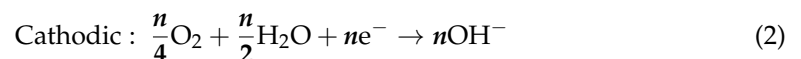
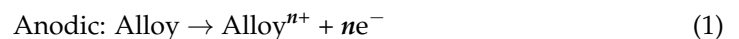
To evaluate the constituents and their related valences of the passivation films on the 304SS and equimolar CoCrFeNi HEA, which were formed in the air, at the first corrosion potential (E_{corr1}) and 0.6 V (vs. Ref) in $0.5 \text{ M H}_2\text{SO}_4$ AAS, the specimens were washed with deionized water and dried before being transferred to the X-ray photoelectron spectroscopy (XPS) analyzer chamber, by using a ULVAC-PHI (Chigasaki, Japan), PHI 5000 VersaProbe/Scanning Electron Spectroscopy for Chemical Analysis (ECSA) Microprobe in conjunction with monochromatic Al $K\alpha$ X-ray radiation with energy 1487 eV . The peaks of XPS data analyzed by XPSPEAK41 were also fitted by the mixed Gaussian–Lorentzian functions after Shirley background subtraction. The binding energy of peaks positions was consulted from NIST XPS Database.

2.4. Inductively Coupled Plasma Mass Spectrometry (ICP-MS)

To observe the dissolving elements on the CoCrFeNi HEA and 304SS in $0.5 \text{ M H}_2\text{SO}_4$ AAS, during polarization measurements and constant potential tests, 15 mL of the solution was taken from the corrosion cell for metal ion quantitative analyses by inductive coupled plasma mass spectrometry (ICP-MS) when the applied potential arrived at E_{corr1} , 0.25 V and 0.6 V (vs. Ref), respectively.

2.5. First-Principles Calculations

Similar to the previous report [28], the electrochemical reactions on the surfaces of alloys in AAS are the following:



The bond energy E_b is defined as below

$$E_b^B = -\frac{1}{n} (E_{\text{OH/Alloy}} - E_{\text{Alloy}} - \frac{n}{2} E_{\text{H}_2\text{O}} - \frac{n}{4} E_{\text{O}_2}) \quad (4)$$

$$E_b^A = -\frac{1}{A} (E_{\text{OH/Alloy}} - E_{\text{Alloy}} - \frac{n}{2} E_{\text{H}_2\text{O}} - \frac{n}{4} E_{\text{O}_2}) \quad (5)$$

where E_b^B is the bond energy per OH bond and E_b^A is the bond one per surface area, n is the total number of electrons escaping from the alloy to form OH^- ions on its surface and n^+ the positive charges left on alloy. Additionally, $E_{\text{OH/Alloy}}$ and E_{Alloy} are the total energies of the corresponding clean alloy slab and additionally containing the ad-layer of n hydroxyl ions on the slab and $E_{\text{H}_2\text{O}}$ and E_{O_2} the energies per H_2O , and O_2 molecule, respectively, positive E_b indicating the exothermic reaction at $T = 0$ K.

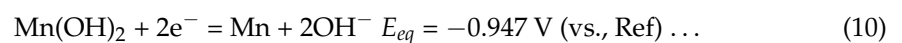
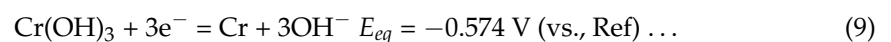
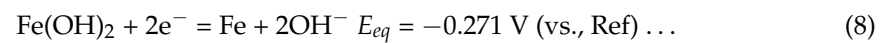
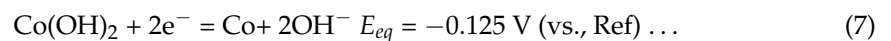
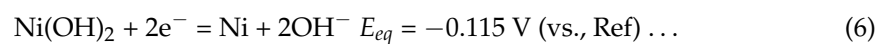
The calculated E_{Alloy} and $E_{\text{OH/Alloy}}$ of CoCrFeNi and 304SS alloy including facets (100), (110), and (111) were conducted by the first-principal method based on DFT. As used in the previous report [29], the technical of special quasi-random structure (SQS) [36,37], the Vienna ab initio simulation program (VASP) [38,39], the projector augmented wave (PAW) method [40,41], and the exchange-correlation function as the generalized gradient approximation (GGA) parameterized by Perdew, Burke, and Ernzerhof (PBE) [42] were also included.

The electrons on semi-core p state were regarded as valence ones. The bulk calculation of alloy plane-wave energy cutoff was carried out by 600 eV with Monkhorst–Pack [43] $4 \times 4 \times 1$ k-point mesh in the slab. The tolerance energy and atomic force were 1.0×10^{-5} and 1.0×10^{-4} eV, respectively, for the fully relaxed position, using SQS supercell composed of 144 atoms for both alloys to optimize the randomness of arrangement. The asymmetric slab composed of several atomic layers including half fixed bottom layers and half fully relaxed outer layers was employed to model all surfaces. For deriving $E_{\text{OH/Alloy}}$, the monolayer hydroxyl ions were set on each facet with the same stacking way as the original alloy layer and a vacuum distance of 12–15 Å from the top surface was assumed to avoid the coupling of consecutive slabs.

3. Result and Discussion

3.1. Electrochemical Corrosion Behaviors Analysis

Figure 1 shows the dynamic polarization curves of equimolar CoCrFeNi HEA and 304SS specimens in 0.5 M H_2SO_4 AAS without pre-immersion, respectively. Table 2 presents the corrosion characteristics derived from Figure 1, including three corrosion potentials (E_{corr1} , E_{corr2} , and E_{corr3}), three corrosion current densities (i_{corr1} , i_{corr2} , and i_{corr3}), the passivation current density (i_{pass}), the first critical current density (i_{crit1}), the second critical current density (i_{crit2}), and the trans-passive potential (E_{trans}). Around E_{corr1} , the metal elements may be initially oxidized into hydroxides on the surface as follows:



where E_{eq} is the calculated reduction-oxidation equilibrium potential of metal and metal hydroxide derived from Nernst equation at $\text{pH} = 0.47$ for 0.5 M H_2SO_4 AAS, also listed in Table 3. The E_{corr1} of 304SS (−354 mV) is lower than that of HEA (−179 mV), consistent with $E_{\text{eq 304SS}}$ (−359 mV) lower than $E_{\text{eq CoCrFeNi}}$ (−305 mV). The less k_{sp} means the more stable hydroxide compound in aqueous solutions. The Cr content should play an important role in the first critical current density (i_{crit1}), because the k_{sp} of $\text{Cr}(\text{OH})_3$ is much less than the other metal hydroxides including $\text{Mn}(\text{OH})_2$, $\text{Ni}(\text{OH})_2$, $\text{Co}(\text{OH})_2$, and $\text{Fe}(\text{OH})_2$, as listed in Table 4 [44]. Both the i_{crit1} and i_{corr1} of CoCrFeNi HEA smaller than 304SS are straightforwardly ascribed to the higher Cr content of the former.

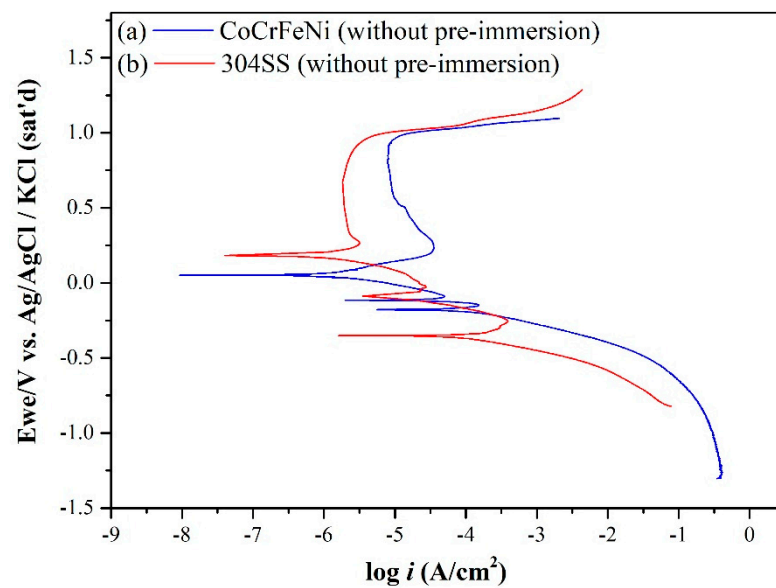


Figure 1. Potentiodynamic polarization curves of (a) CoCrFeNi HEA and (b) 304SS without pre-immersion in 0.5 M H₂SO₄ (pH = 0.47) AAS.

Table 2. Corrosion characteristics derived from polarization curves shown in Figure 1.

	CoCrFeNi HEA (without Immersion)			CoCrFeNi HEA (Immersion for 30 min)	304SS		
	1st	2nd	3rd	5	1st	2nd	3rd
E_{corr} (mV)	−179	−116	52	5	−354	−87.9	183.2
i_{corr} ($\mu\text{A}/\text{cm}^2$)	50.2	16.2	2.14	1.4	143.5	8.4	2.3
E_{trans} (mV)	982			963	981		
i_{pass} ($\mu\text{A}/\text{cm}^2$)	7.94			4.8	1.83		
i_{crit} ($\mu\text{A}/\text{cm}^2$)	1st	2nd		42.7	1st	2nd	
	152.8	35.5			390.8	3.2	

Since the k_{sp} values of iron (II), Mn(II) and cobalt(II) hydroxides are dramatically reduced from 2×10^{-13} and 3×10^{-16} to 6×10^{-38} and 1×10^{-43} for iron(III) and cobalt(III) ones, listed in Table 4 [40]. Fe, Co, Mn and Ni, beside Cr, may also play a role in the passivation zone by the following electrochemical reactions:

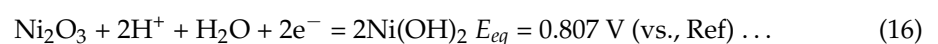
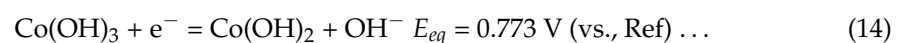
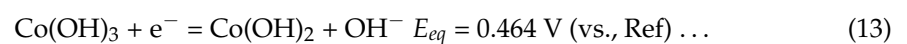
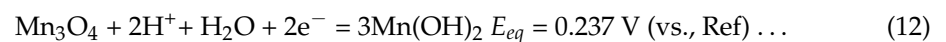
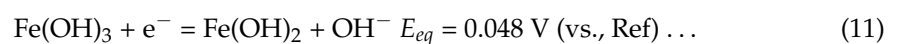


Table 3. The calculated reduction-oxidation equilibrium potentials of metal and metal hydroxides (E_{eq}) by Equations (6)–(10) and that (E'_{eq}) of metal and metal ions by Nernst equation, assuming metal ions activity at 10^{-6} M at pH = 0.47 in 0.5 M H₂SO₄ AAS for CoCrFeNi HEA and 304SS.

Metal-Metal hydroxides	
$E_{eq\ CoCrFeNi} = -0.305$ V (Ag/AgCl)	
$E_{eq\ 304SS} = -0.359$ V (Ag/AgCl)	
Metal-Metal ion	
Co = Co ²⁺ + 2e ⁻	$E'_{eq} = -0.457$ V _{SHE}
Cr = Cr ³⁺ + 3e ⁻	$E'_{eq} = -0.864$ V _{SHE}
Fe = Fe ²⁺ + 2e ⁻	$E'_{eq} = -0.627$ V _{SHE}
Ni = Ni ²⁺ + 2e ⁻	$E'_{eq} = -0.430$ V _{SHE}
Mn = Mn ²⁺ + 2e ⁻	$E'_{eq} = -1.356$ V _{SHE}
Si + 3H ₂ O = H ₂ SiO ₃ + 4H ⁺ + 4e ⁻	$E'_{eq} = -1.096$ V _{SHE}
$E'_{eq\ CoCrFeNi} = -0.675$ V _{SHE} = -0.831 V (Ag/AgCl)	
$E'_{eq\ 304\ SS} = -0.694$ V _{SHE} = -0.900 V (Ag/AgCl)	

Table 4. Constants of solubility product k_{sp} for hydroxides of Co, Cr, Fe, Ni, and Mn [41].

Compound	k_{sp}	Compound	k_{sp}
Co(OH) ₂	3×10^{-16}	Fe(OH) ₂	2×10^{-15}
Co(OH) ₃	1×10^{-43}	Fe(OH) ₃	6×10^{-38}
Cr(OH) ₃	7×10^{-31}	Ni(OH) ₂	2×10^{-16}
Mn(OH) ₂	2×10^{-13}	Mn(OH) ₃	1×10^{-36}

However, Ni(OH)₂ could not be further oxidized in reaction (16) at the potential below 0.8 V, keeping its k_{sp} value of 2×10^{-16} , much greater than those of iron (III) and cobalt (III) hydroxides. The more Fe and Co content in the passivation film, the more anti-corrosion ability the alloy has, while the former in reaction (11) occurs at a lower potential than the latter in reaction (14). This means that the more Fe content in the alloy, the lower the potential for initiating and stabilizing passivation, and the less Ni content in the alloy, the more stable the passivation film, also resulting in less i_{pass} and i_{crit2} for 304SS than that for CoCrFeNi HEA in 0.5 M H₂SO₄ AAS, as shown in Figure 1 and listed in Table 2.

The E_{corr1} (−0.354 V) of 304SS is very close to $E_{eq\ 304SS}$ (−0.359 V) calculated in Table 3, indicating some more active reactions should be considered such as metal–metal ion ones below or around E_{corr1} , as listed the lower parts in Table 3 with the calculated reduction-oxidation equilibrium potential (E'_{eq}) for the metal–metal ion reactions. It should be noticed that the E'_{eq} for alloys cannot be directly added or subtracted [45]; they should be first transformed to Gibbs energy by $\Delta G = -nFE'_{eq}$. Assuming all the metal ionic activities are 10^{-6} M, the potential-pH diagrams [46] show Co as Co²⁺, Cr as Cr³⁺, Fe as Fe²⁺, Ni as Ni²⁺, Mn as Mn²⁺ and Si as H₂SiO₄ at the corrosion potentials of CoCrFeNi HEA and 304SS with pH = 0.47 in 0.5 M H₂SO₄ AAS. According to E'_{eq} of the individual alloying elements as listed in Table 3, the calculated equilibrium potentials of CoCrFeNi HEA ($E'_{eq\ CoCrFeNi}$) and 304SS ($E'_{eq\ 304SS}$) in 0.5 M H₂SO₄ AAS are derived as follows:

$$E'_{eq\ CoCrFeNi} = [(-0.457 \times 2 \times 24.36/100) + (-0.864 \times 3 \times 26.85/100) + (-0.627 \times 2 \times 25.18/100) + (-0.430 \times 2 \times 23.61/100)] \div 226.85/100 = -0.634$$
 VSHE = -0.831 V (vs., Ref) ... (17)

$$E'_{eq\ 304SS} = [(-0.627 \times 2 \times 68.65/100) + (-0.864 \times 3 \times 20.65/100) + (-0.430 \times 2 \times 7.5/100) + (-1.356 \times 2 \times 2.12/100) + (-1.096 \times 4 \times 1.08/100)] \div 222.81/100 = -0.703 \text{ VSHE} = -0.900 \text{ V (vs., Ref)} \dots \quad (18)$$

These two calculated reduction-oxidation (metal–metal ions) equilibrium potentials (E'_{eq}) of CoCrFeNi and 304SS are also listed in Table 3. Similarly, $E'_{eq\ 304SS}$ is lower than $E'_{eq\ CoCrFeNi}$. The potentiodynamic curves are decomposed into anodic curves and cathodic curves around the mixed potentials by Tafel region slopes and the diffusion limiting current density of O_2 as shown in Figure 2a for CoCrFeNi HEA and Figure 2b for 304SS. Figure 2 presents the anodic curves and cathodic curves intersecting three times, thus revealing three corrosion potentials (E_{corr}), two critical current densities (i_{crit}), and three corrosion current densities (i_{corr}). However, not only the greater i_{crit1} but also the wider active potential range is found for 304SS, meaning it is harder to be passivated around this region. In contrast, the anodic curves and cathodic curves only intersect one time for CoCrFeNi HEA with pre-immersion for 30 min before the test, as shown in Figure 3a, indicating that the CoCrFeNi HEA was further passivated to reduce the first critical current density (i_{crit1}) to be less than the cathodic reaction one. The related corrosion characteristics are listed in Table 2, revealing less i_{corr} and i_{pass} than the specimen without immersion. The potentiodynamic curve of 304SS with pre-immersion for 30 min is shown in Figure 3b, similar to Figure 2b. Figure 4 shows the current density variations of CoCrFeNi HEA and 304SS at a constant potential of 0.6 V for 2 h. Consistent with the results of i_{pass} , the current density of the latter is much less than that of the former, also indicating that the passivation film of the latter is more stable than that of the former at 0.6 V, ascribed to Fe(III) and Mn(III) with the much lower k_{sp} already formed in reactions (11), (12) and (13) while this was not yet the case for Co(III) and Ni(III) in reactions (14) and (16). The SEM observations of CoCrFeNi HEA and 304SS are shown in Figure 5a before and Figure 5b after potentiodynamic tests, indicating deeper grain boundary corrosion and more corrosion products for CoCrFeNi HEA than 304SS.

(a)

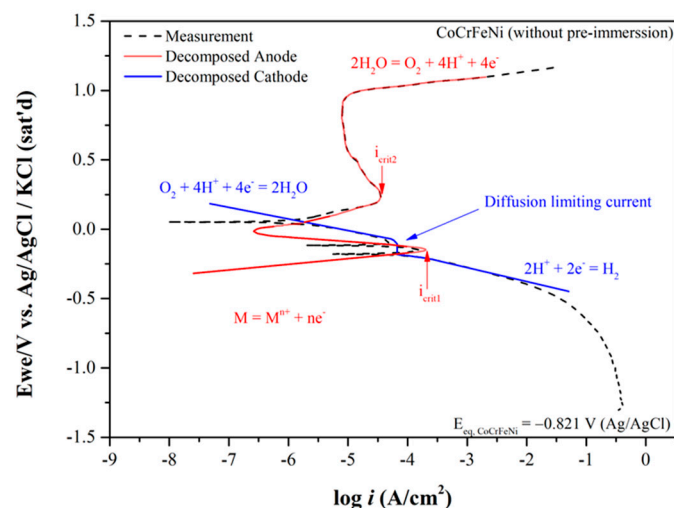


Figure 2. Cont.

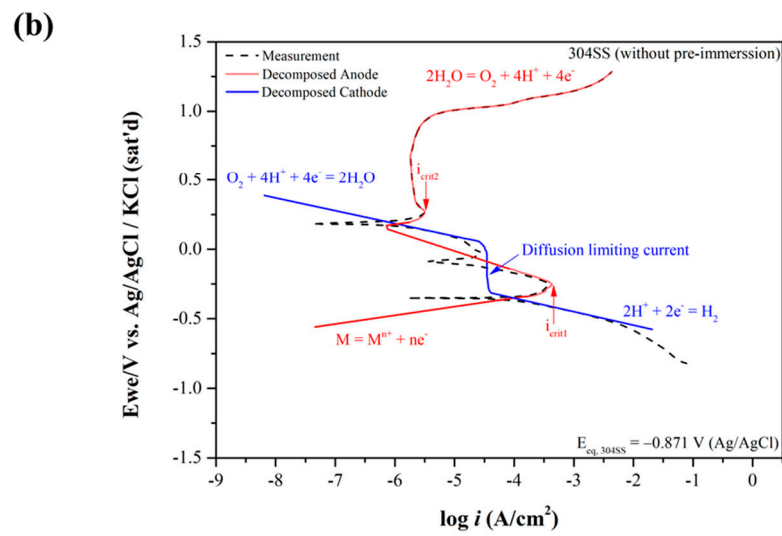


Figure 2. The anodic curves and cathodic curves decomposed from Figure 1 for (a) CoCrFeNi HEA and (b) 304SS.

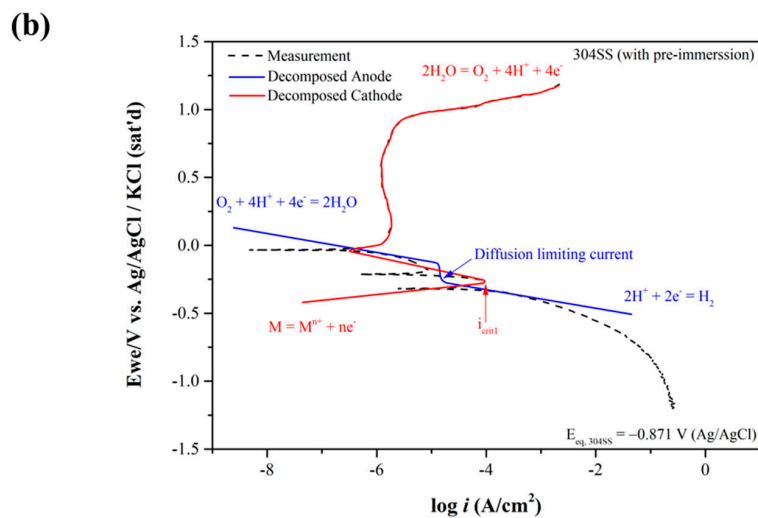
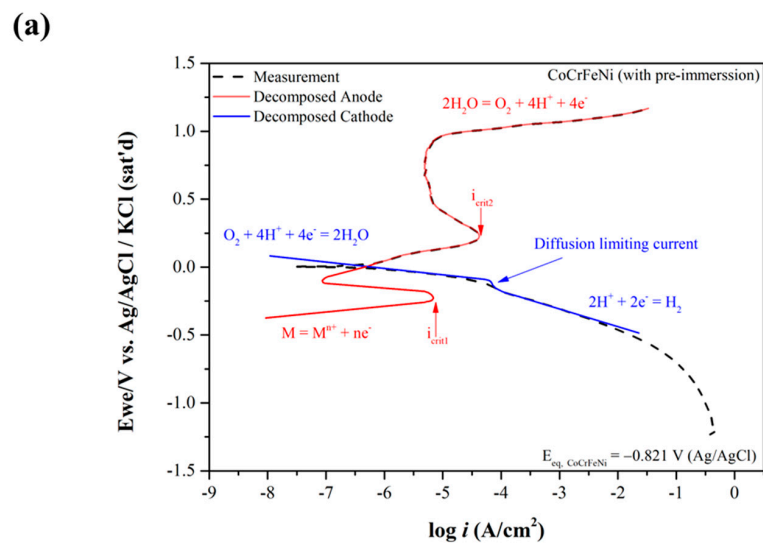


Figure 3. Dynamic polarization curves of (a) CoCrFeNi HEA and (b) 304SS with pre-immersion for 30 min, also decomposed into the anodic and cathodic ones.

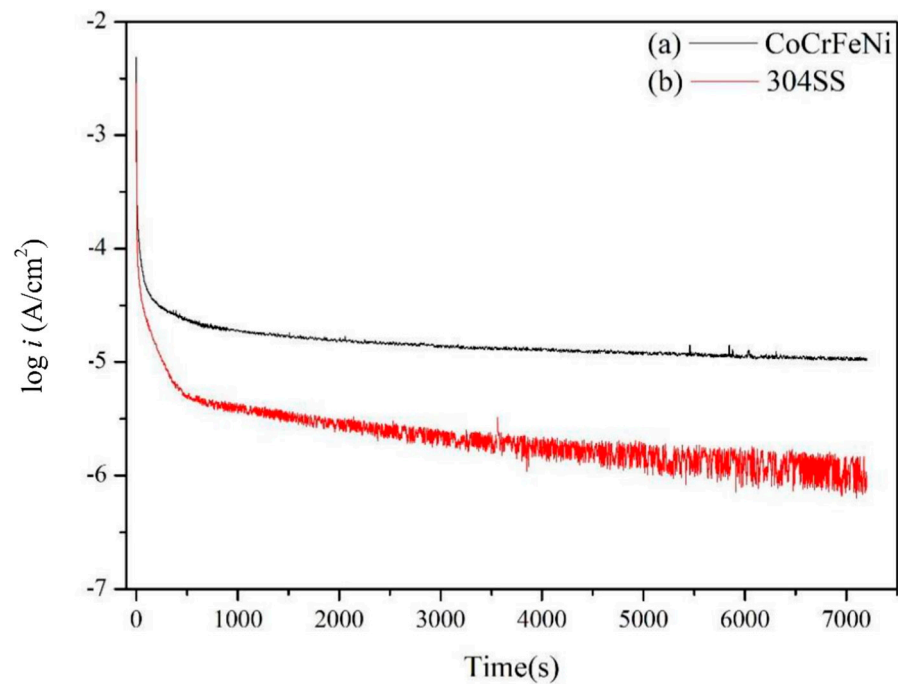


Figure 4. Current densities of (a) CoCrFeNi HEA and (b) 304SS at constant potential 0.6 V for 2 h.

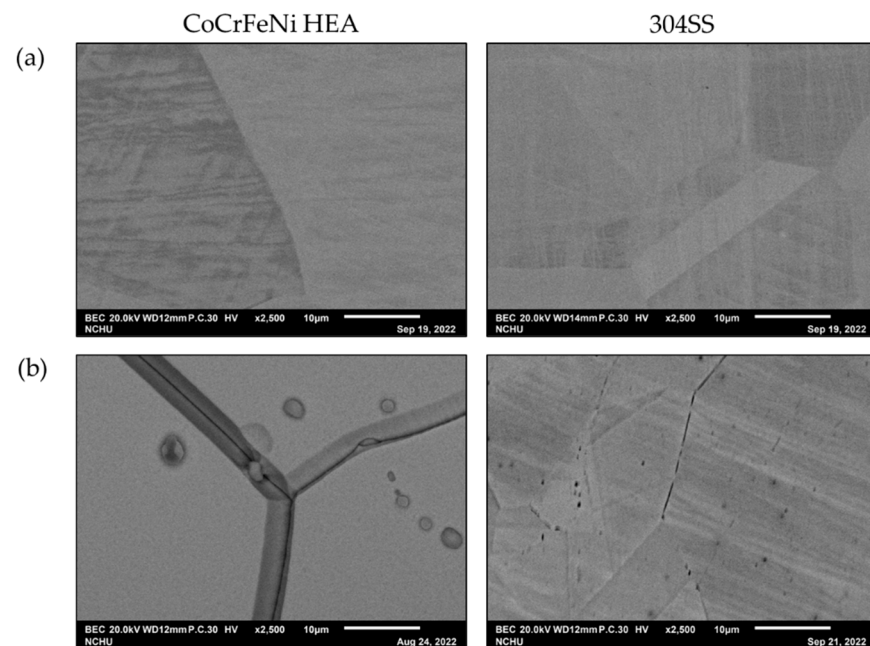


Figure 5. SEM observations of CoCrFeNi HEA and 304SS (a) before and (b) after potentiodynamic tests.

3.2. Characteristics of the Passivation Films by X-ray Photoelectron Spectroscopy

Figure 6 presents the atomic proportion variations (within 0.5% error) of metal elements in the passive film for both alloys derived from XPS analyses. Quite different from the matrix of CoCrFeNi HEA, Co is the major component of passivation film in the air but decreases with the increasing potential, while Cr increases with the increasing potential and becomes the major one at 0.6 V. Ni keeps the least one. Fe in the air for HEA is a little less than that at E_{corr1} (−0.18V), which is higher than that of 304SS, especially for the immersion ones, leading to a greater ratio of stable ferric compound. Fe is the major component of passivation film in the air for 304SS, while it is replaced by Cr at E_{corr1} (−0.35 V) and they

are almost equal at 0.6 V. Ni and Mn are always the minor components and gradually decrease with the increasing potential, while the ratio of Mn in the passivation film is greater than that in metal matrix, resulting from E_{eq} in reaction (10) being much lower than the others.

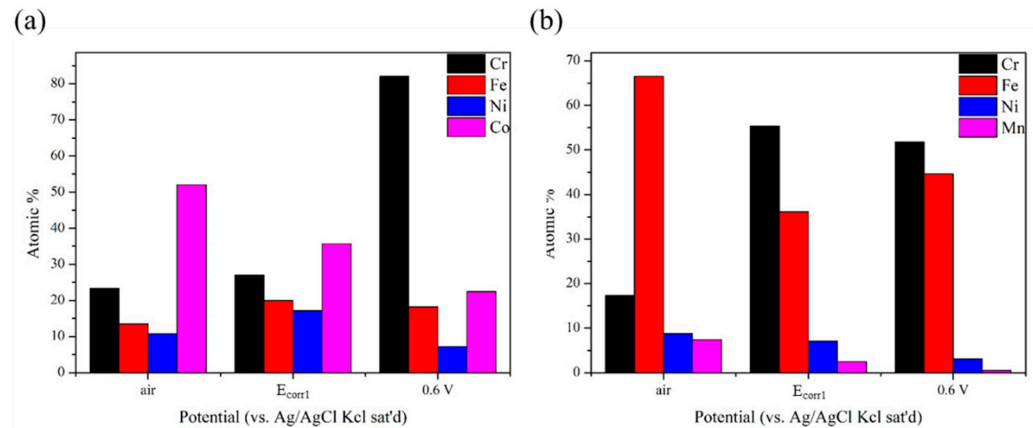


Figure 6. The atomic proportion variations (within 0.5% error) of metal elements in the passive films formed in air, at E_{corr1} and 0.6 V for (a) CoCrFeNi HEA and (b) 304SS specimens, derived from XPS.

Figures 7 and 8 show the detailed XPS results of Cr 2p_{3/2}, Fe 2p_{3/2}, Ni 2p_{3/2}, Co 2p_{3/2}, Mn 2p_{3/2}, and O 1s for the CoCrFeNi HEA and 304SS passivation films in the air, at E_{corr1} and at 0.6 V passivation potential in 0.5 M H₂SO₄ AAS respectively. In Figures 7a and 8a, the Cr 2p_{3/2} ionization is separated into several constituent peaks representing the metallic Cr⁰ (574 eV), Cr₂O₃ (576.1 eV), and Cr(OH)₃ (577.2 eV). Element Cr in 304SS and CoCrFeNi HEA is primarily passivated to chromium hydroxide and oxide in 0.5 M H₂SO₄ AAS. Figures 7b and 8b show that the Fe 2p_{3/2} ionization is split into several constituent peaks representing the metallic Fe⁰ (706.7 eV), Fe/Ni (707.2 eV), Fe₃O₄ (708.1 eV), FeO (709.6 eV), Fe₂O₃ (711.6 eV) and Fe(OH)O (711.9 eV). In Figure 7b at −0.18 V, more Fe in the CoCrFeNi HEA is oxidized to Fe(OH)O earlier than 304SS, due to the higher E_{corr1} of the former. The ferric states in both films are the main components of the iron at 0.6 V, resulting in the stable passivation regions. As shown in Figures 7c and 8c, the Ni 2p_{3/2} spectra are split into three constituent peaks representing the metallic Ni⁰ (852.7 eV), NiO (853.6 eV), and Ni(OH)₂ (858.6 eV). The results show that the nickel on both alloys is not further oxidized to high-valence nickel such as Ni₂O₃ or NiO₂ for reducing the solubility of nickel in 0.5 M H₂SO₄ AAS. In Figure 7d, not similar to iron, just a small part of cobalt on CoCrFeNi HEA is further oxidized into Co(OH)O at 0.6 V, a smaller k_{sp} that can also increase the corrosion resistance, revealing the enhanced passivation at potentials higher than 0.6 V. Peaks of MnO (640.8 eV) are observed on 304SS in air and at E_{corr1} (−0.35 V), then further oxidized into Mn₃O₄, Mn₂O₃ and MnO₂, as shown in Figure 8d, basically compliant with reactions (12), (13) and (15). The O 1s spectra are separated into two or three peaks, as shown in Figures 7e and 8e. The O^{2−} species (530.2 eV) are from the metal oxides. The peak at 531.5 eV represents the metal hydroxides and the peak at 532.8 eV corresponds to a little H₂O coming from the hydrated oxides as shown in Figure 8e at 0.6 V. Cr₂O₃ is formed in the air for 304SS, then is hydroxylated at E_{corr1} , and much more hydroxyl is formed at 0.6 V. On the other hand, the passive film for CoCrFeNi HEA is thin enough to obviously detect metal Cr, compared with 304SS where the small metal signal is detected at 0.6 V. The hydroxylation of Fe oxide occurs at 0.6 V for 304SS while it occurs at E_{corr1} for HEA, possibly by the following reactions:



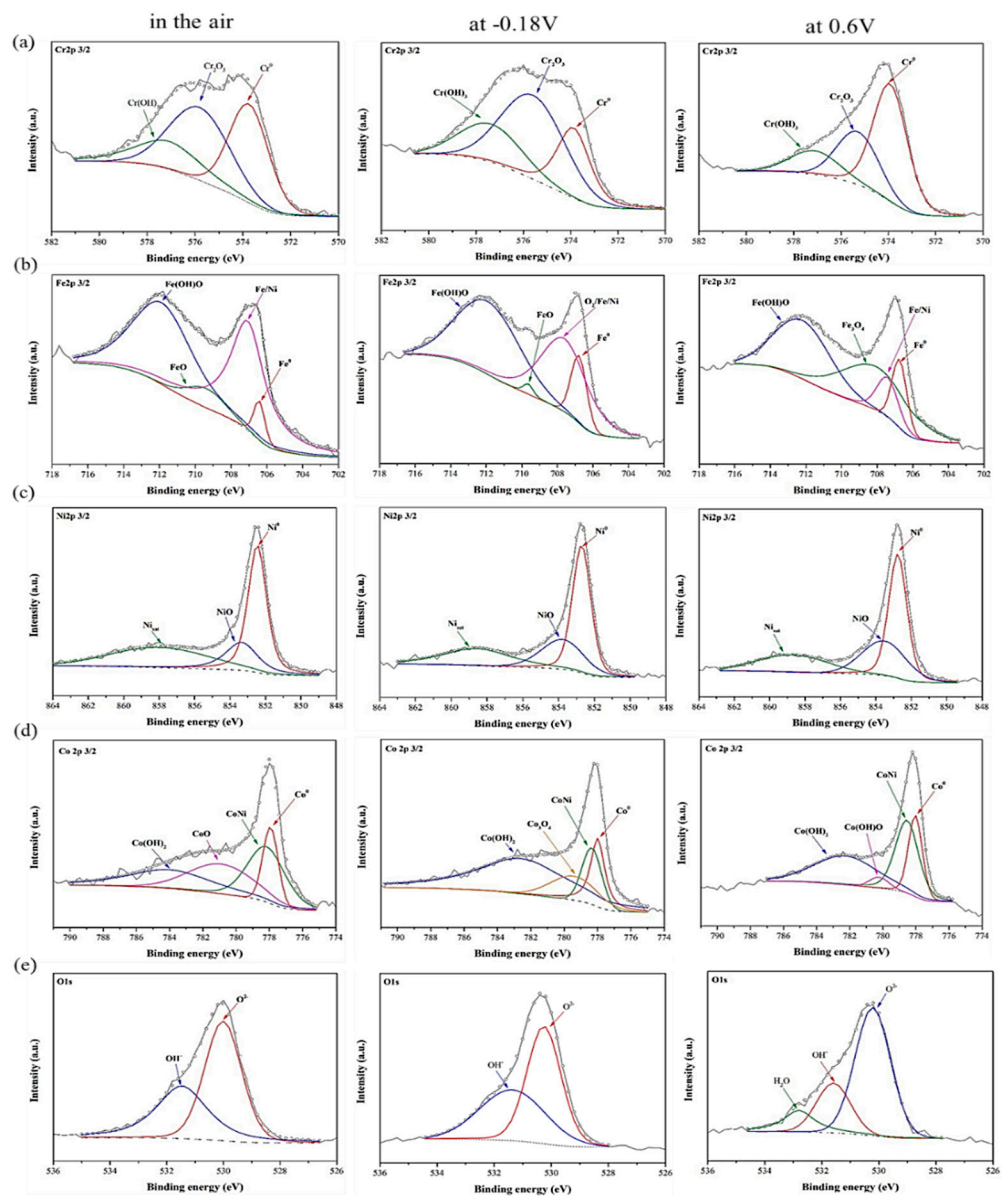


Figure 7. High resolution XPS spectra of the passivation films formed in the air, at E_{corr1} ($-0.18V$) (Ag/AgCl) and at $0.6V$ (Ag/AgCl) in $0.5M H_2SO_4$ AAS, (a) Cr $2p_{3/2}$, (b) Fe $2p_{3/2}$, (c) Ni $2p_{3/2}$, (d) Co $2p_{3/2}$ and (e) O $1s$ on the surface of CoCrFeNi HEA.

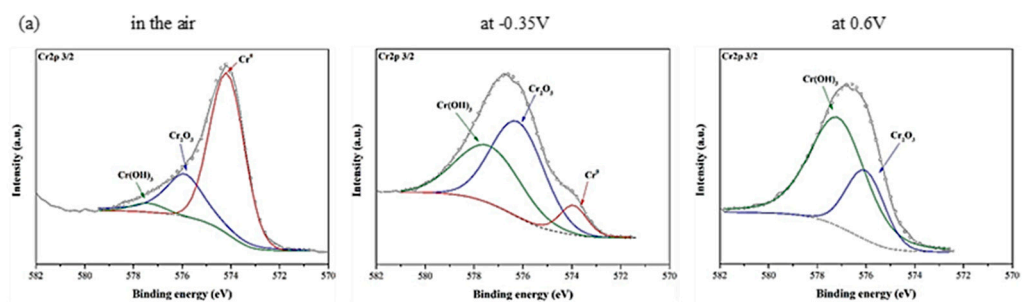


Figure 8. Cont.

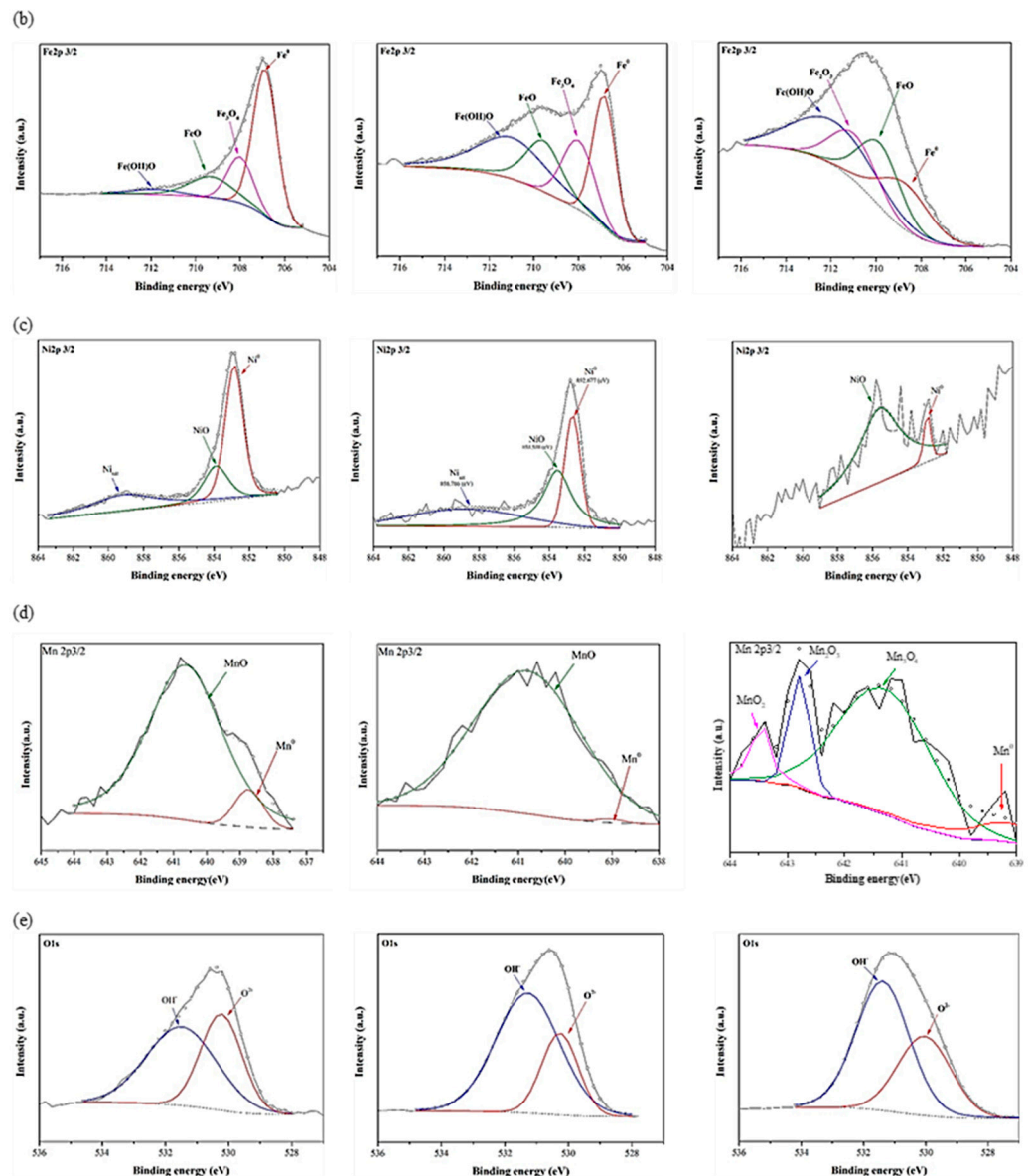


Figure 8. High resolution XPS spectra of the passivation films formed in the air, at E_{corr1} (-0.35 V) (Ag/AgCl) and 0.6 V (Ag/AgCl) in 0.5 M H_2SO_4 AAS. (a) Cr $2p_{3/2}$, (b) Fe $2p_{3/2}$, (c) Ni $2p_{3/2}$, (d) Mn $2p_{3/2}$ and (e) O $1s$ on the surface of 304SS.

A small ratio of Ni is oxidized into NiO for both CoCrFeNi HEA and 304SS. The content ratio of $Cr(OH)_3$ to Cr_2O_3 is enhanced and the peak height (content) of Cr^0 is reduced by the passivation for 304SS. Similar results are found for the enhanced ratio of $Fe(OH)O$ to FeO and Fe_3O_4 . However, they both vary scarcely for CoCrFeNi HEA. The reduced contents of Fe^0 , Cr^0 , and Ni^0 for CoCrFeNi are much less than that for 304SS, indicating that the passivation film of the latter is thicker than that of the former at 0.6 V. The thicker the passivation film, the slower the mass transportation of the metal ion is, supporting the lower i_{pass} of 304SS. The peaks of Ni and NiO are getting weaker by the passivation for both alloys. The content ratio of $Co(OH)_2$ to CoO or Co_3O_4 is also enhanced at E_{corr1} as shown in Figure 7d. Although $Co(OH)O$ was found at 0.6 V, the major phase is $Co(OH)_2$, consistent with the calculated potential indicated in reactions (7) and (14). The peak ratio of OH^- to O^{2-} is enhanced as well at E_{corr1} and 0.6 V for 304SS, caused by the enhanced $Cr(OH)_3$ and $Fe(OH)O$, while it is not for CoCrFeNi HEA, but a small peak of H_2O is observed due to the hydrated oxides.

3.3. The Concentration of Dissolved Elements

Table 5 presents the dissolved ion concentrations of Co, Cr, Fe, Ni, and Mn for (a) CoCrFeNi and (b) 304SS specimens dynamically polarized from -1.2 V to E_{corr1} 0.25 V and 0.6 V (vs. Ref) in 0.5 M H_2SO_4 AAS, intermittently analyzed by ICP-MS during the polarization measurement. The i_{pass} of CoCrFeNi shown in Figure 1 is greater than 304SS, but the total amount of ion releasing from CoCrFeNi at E_{corr1} , 0.25 V or 0.6 V is significantly less than 304SS as listed in Table 5. The E_{corr1} of 304SS is -0.354 V, which is very close to the E_{eq} of metals hydroxides for 304SS (-0.359 V). This means that reactions between metals and metal ions listed in Table 3 should be considered. In other words, the stable hydroxides of 304SS have not been completely formed yet at the E_{corr1} of 304SS since Cr and Mn hydroxides could be formed individually while the others are not yet as indicated in reactions (6), (7), (8), (9) and (10). Furthermore, the k_{sp} of $Mn(OH)_2$ is much higher than those of other metal hydroxides, resulting in the large amount of Mn ion releasing from 304SS to the solution at E_{corr1} and leading to the greater increment and greater increasing ratio for Cr, Fe, Ni ions from E_{corr1} to 0.25 V before the passivation, corresponding to the greater i_{corr1} and i_{crit1} , and the wider active range than CoCrFeNi shown in Figure 2a. However, the ion concentration increasing ratio from 0.25 V to 0.6 V of 304SS is much lower than that from E_{corr1} to 0.25 V since reactions (11), (12), (13) and (15) occur to form Fe(III) and Mn(III or IV) with much lower k_{sp} , as listed in Table 4, and further stabilize the passivation film for retarding the leaching out of Fe and Mn ions as shown in Figure 6a, corresponding to the lower i_{pass} and i_{crit2} . Obviously, most ions from 304SS were released during the polarization from -1.2 V to 0.25 V. On the other hand, the ion concentration increasing ratio of Ni or Co from 0.25 V to 0.6 V for CoCrFeNi HEA is still greater than that from E_{corr1} to 0.25 V since reactions (14) and (16) do not yet proceed and the leaching out of Co and Ni is still obvious, as revealed in Figure 6b, corresponding to the greater i_{crit2} and i_{pass} .

Table 5. The dissolved ion concentrations (ppt) of 304SS and (CoCrFeNi HEA at the potentials of E_{corr1} , 0.25 V and 0.6 V in 0.5 M H_2SO_4 AAS, derived from ICP-MS.

	304SS			
	Cr	Fe	Ni	Mn
E_{corr1}	4.3×10^2	5.6×10^3	8.0×10^2	5.9×10^3
0.25 V	3.7×10^4	1.6×10^5	1.6×10^4	1.2×10^4
0.6 V	5.0×10^4	2.1×10^5	2.0×10^4	1.4×10^4
Increment from E_{oc1} to 0.25 V	3.6×10^4	1.6×10^5	1.5×10^4	5.8×10^3
Increase ratio from E_{oc1} to 0.25 V	85	28	19	0.99
Increment from 0.25 V to 0.6 V	1.3×10^3	4.6×10^4	3.7×10^3	2.0×10^3
Increase ratio from 0.25 V to 0.6 V	0.35	0.28	0.23	0.18
	CoCrFeNi HEA			
	Cr	Fe	Ni	Co
E_{corr1}	3×10^2	8.3×10^2	3.2×10^2	9.1×10
0.25 V	5.2×10^2	3.8×10^3	9.9×10^2	6.9×10^2
0.6 V	6.9×10^2	7.3×10^3	6.4×10^3	6.0×10^3
Increment from E_{oc1} to 0.25 V	2.2×10^2	3×10^3	6.8×10^2	6.0×10^2
Increase ratio from E_{oc1} to 0.25 V	0.72	3.57	2.14	6.57
Increment 2 from 0.25 V to 0.6 V	1.7×10^2	3.5×10^3	5.4×10^3	5.3×10^3
Increase ratio from 0.25 V to 0.6 V	0.33	0.93	5.46	7.76

3.4. First-Principles Calculations

Based on the composition derived from EDS data listed in Table 1, the 304SS FCC slab is composed of $\text{Cr}_{27}\text{Fe}_{99}\text{Ni}_{13}\text{Mn}_3\text{Si}_2$ 144 atoms and the HEA one is composed of $\text{Co}_{36}\text{Cr}_{36}\text{Fe}_{36}\text{Ni}_{36}$ 144 atoms with 18 hydroxyl ions on the (100) facet, 12 hydroxyl ions on the (110) facet and 16 hydroxyl ions on the (111) facet. The optimized atomic geometries of (100), (110), and (111) orientations are shown in Figures 9 and 10 for three facets of 304SS and HEA.

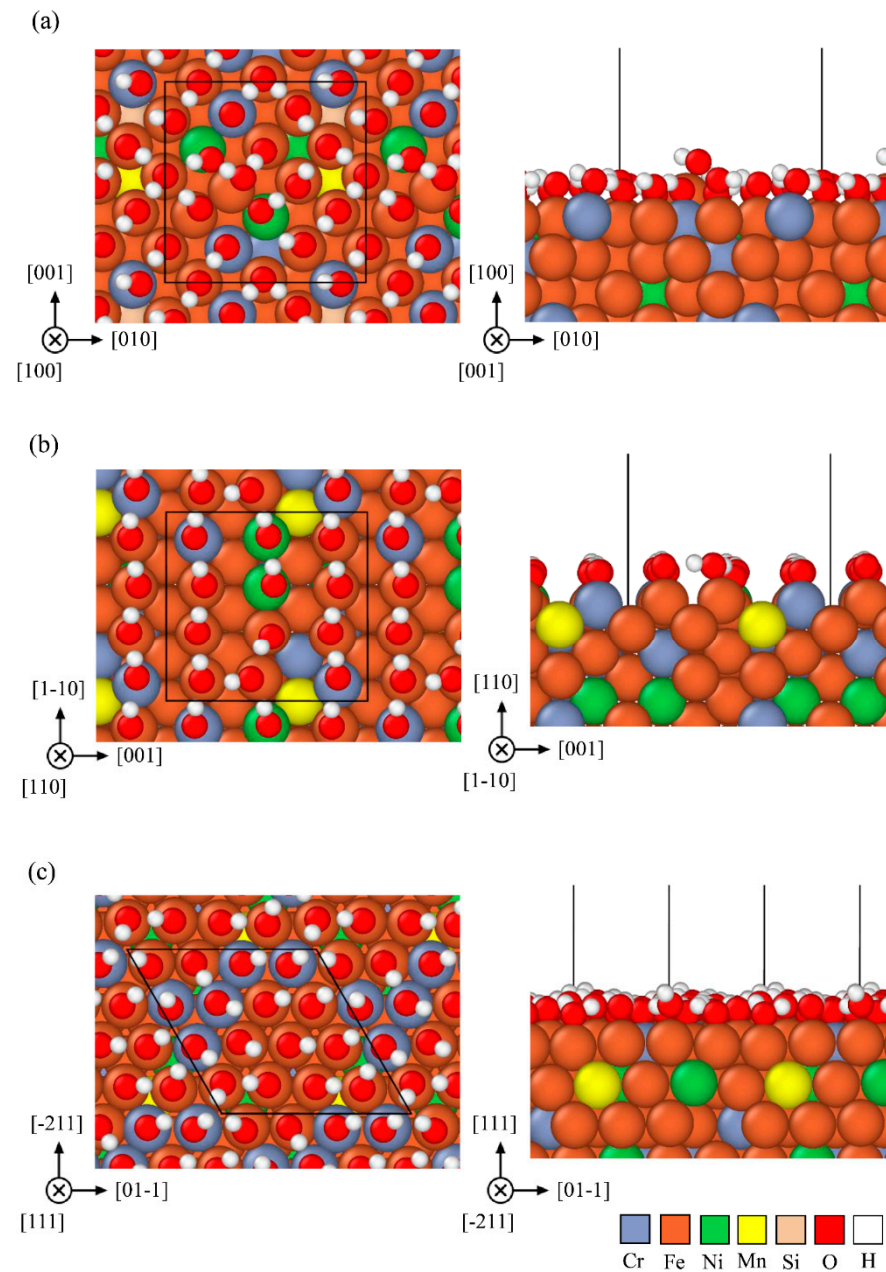


Figure 9. Top and side views of the atomic geometry of monolayer OH on facets (a) (100) (b) (110), and (c) (111) of FCC structure for 304SS specimens derived from the first-principles calculations.

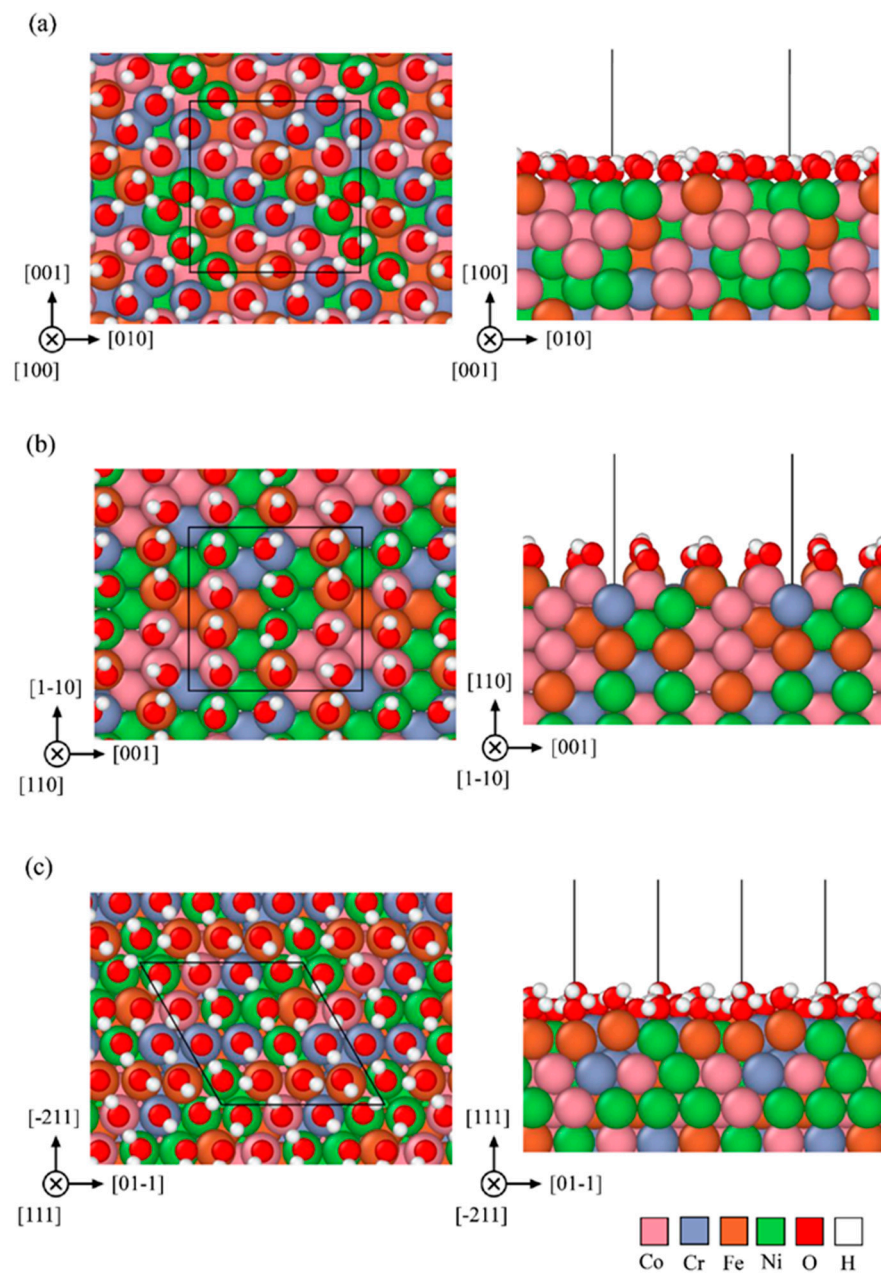


Figure 10. Top and side views of the atomic geometry of monolayer OH on facets (a) (100) (b) (110), and (c) (111) of FCC structure for CoCrFeNi specimens derived from the first-principles calculations.

The calculated E_b^B and E_b^A of monolayer hydroxyl on three facets for 304SS and CoCrFeNi HEA are listed in Table 6, according to equations (4) and (5). The average E_b value of 304SS is greater than that of CoCrFeNi HEA. Obviously, the E_b values of monolayer hydroxyl ion adsorbed on the (100), (110), and (111) facets of CoCrFeNi HEA calculated by the first principle are less than the those of 304SS in terms of either per OH bond or per area. Meanwhile, the connecting morphology of the hydrogen bond is found to be denser and more uniform on all facets for 304SS than those for HEA, as shown in Figures 9 and 10. The least E_b per OH bond is 1.186 eV, found on the (111) facet of CoCrFeNi HEA and the least one per area is 0.1845 eV, found on the (110) facet of CoCrFeNi HEA. In other words, facet (111) or (110) of the CoCrFeNi HEA is less stable and preferentially corroded in AAS, consistent with the worse performances around the passivation region for equimolar CoCrFeNi HEA. It is straightforward that the higher E_b of hydroxyl absorbed on the 304SS is responsible for the better corrosion resistance around the passivation region in

0.5 M H₂SO₄ AAS to retard the mass transportation and/or the leaching out of metal ions, leading to the lower i_{crit2} and i_{pass} for 304SS, as listed in Table 2 or illustrated in Figure 1.

Table 6. Average bond energy per bond (E_b^B) and per area (E_b^A) for monolayer OH on facets (100), (110), and (111) of FCC structure for 304SS and CoCrFeNi HEA.

Facets of 304SS (Cr ₂₇ Fe ₉₉ Ni ₁₃ Mn ₃ Si ₂)	E_b^B	E_b^A
FCC (100) (144 + 18 OH)	1.7982	0.2866
FCC (110) (144 + 12 OH)	1.9843	0.2229
FCC (111) (144 + 16 OH)	1.4342	0.2631
Average	1.7389	0.2575
Facets of HEA (Co ₃₆ Cr ₃₆ Fe ₃₆ Ni ₃₆)	E_b^B (eV/OH)	E_b^A (eV/Å ²)
FCC (100) (144 + 18 OH)	1.4242	0.2273
FCC (110) (144 + 12 OH)	1.6362	0.1845
FCC (111) (144 + 16 OH)	1.1862	0.2189
Average	1.4156	0.2103

The individual k_{sp} and E_{eq} of each metal hydroxide should be responsible for the stability of the passive film, as discussed previously by comparing with one another while neglecting the interactions of nearby elements and the geometry of hydroxyl ions adsorbed on the metal surface. In contrast, the component, the random arrangement, the coordination, and the facet orientation are all considered and calculated in general by the first-principals calculations.

4. Conclusions

The potentiodynamic curves are decomposed into anodic curves and cathodic curves around the mixed potentials by Tafel region slopes and the diffusion-limiting current density of O₂. The decomposed anodic curves and cathodic curves intersect three times, thus revealing three corrosion potentials (E_{corr}), two critical current densities (i_{crit}), and three corrosion current densities (i_{corr}). The potentiodynamic curve of 304SS with pre-immersion for 30 min is similar to that without pre-immersion, leading to the great amount of ion release. In contrast, the anodic and cathodic curves only intersect one time for CoCrFeNi HEA with pre-immersion for 30 min before the test, as shown in Figure 3a, indicating that the CoCrFeNi HEA was further passivated to reduce the first critical current density (i_{crit1}) to be less than the cathodic reaction one, resulting in the lesser amount of ion release. Additionally, not only the greater i_{crit1} but also the wider active potential range is found for 304SS, meaning that it is harder to be passivated around this region and reactions between metals and metal ions should be mainly considered. The Cr content and the ferric percentage should play an important role on the i_{crit1} because the k_{sp} of Cr(OH)₃ or Fe(OH)₃ is much less than the other metal hydroxides, including Mn(OH)₂, Ni(OH)₂, Co(OH)₂, and Fe(OH)₂. Both i_{crit1} and i_{corr1} of CoCrFeNi HEA are smaller than those of 304SS and are straightforwardly ascribed to the higher Cr content and greater ferric percentage of the former caused by higher E_{corr1} .

The i_{pass} of 304SS is less than that of CoCrFeNi HEA. In other words, the chemical or physical state of a passivation film on 304SS at 0.6 V should be more stable than that on CoCrFeNi, supported by the average bond energy calculation from DFT and the thicker passivation film derived from XPS, leading to the slower diffusion and/or migration rates

of ions in the passivation film. According to the equilibrium potentials of reactions (11) and (16), the less Ni content in the alloy, the more stable passivation film, and the more Fe content in the alloy, the lower the potential for initiating and stabilizing passivation, also resulting in the smaller i_{pass} and i_{crit2} for 304SS than those for CoCrFeNi HEA in 0.5 M H₂SO₄ AAS.

Fe is the major component of passivation film in the air for 304SS, while it is replaced by Cr at E_{corr1} and they are almost equal at 0.6 V, resulting from the much-reduced k_{sp} from the ferrous state to the ferric one. Ni and Mn are always the minor component and gradually decrease with the increasing potential due to their greater k_{sp} of Ni(II) and Mn(II) hydroxides. Quite different from the matrix of CoCrFeNi HEA, Co is the major component of passivation film in the air but decreases with the increasing potential since the equilibrium potential in reaction (12) is higher than 0.6 V, while Cr increases with the increasing potential and becomes the major one at 0.6 V. Ni keeps the least one. Unlike 304SS, Fe in the passive film formed at E_{corr1} is a little more than that in the air, since the E_{corr1} of CoCrFeNi HEA is higher than that of 304SS and prefers to form a more stable and higher ratio ferric compound.

Convincingly, E_b^B and E_b^A resulting from reactions (4) and (5) are also the key indications of thermodynamic stability for the passive film formed on alloys. The E_b of monolayer hydroxyl ion adsorbed on the (111) and (110) facets of CoCrFeNi HEA calculated by the first principle is the least one in terms of per OH bond and per area, respectively, consistent with the worse performances around the passivation region such as the greater i_{crit2} and i_{pass} . Conversely, the hydroxyl ions completely leaning on the surface and uniformly connecting with each other by hydrogen bonds leading to the greater E_b can densify the passivation film to retard the mass transportation and/or the leaching out of metal ions, revealing the lower i_{crit2} and i_{pass} for 304SS. The individual k_{sp} and E_{eq} of each hydroxide formed on the alloy should be related to the stability during the potentiodynamic polarization while the effects of various nearby elements and the geometry of each facet coupled with a hydroxyl layer are not considered. In contrast, the component, the random arrangement of each atom, the crystal orientation, and the connecting geometry of the hydroxyl adsorbed on each facet are completely deliberated in the first principals calculation, and are likely to be more universal and precise for the evaluation around the passivation region.

Author Contributions: Conceptualization, C.-C.Y. and S.-K.Y.; Methodology, C.-C.Y., T.-L.T., B.-W.W., Y.-C.L., M.-H.T. and S.-K.Y.; Software, C.-C.Y. and Y.-C.L.; Validation, C.-C.Y. and S.-K.Y.; Formal Analysis, C.-C.Y., T.-L.T., B.-W.W. and S.-K.Y.; Investigation, C.-C.Y., T.-L.T., B.-W.W. and S.-K.Y.; Resources, C.-C.Y., Y.-C.L., M.-H.T. and S.-K.Y.; Data Curation, C.-C.Y., T.-L.T., B.-W.W. and S.-K.Y.; Writing—Original Draft Preparation, C.-C.Y., T.-L.T., B.-W.W. and S.-K.Y.; Writing—Review & Editing, C.-C.Y. and S.-K.Y.; Visualization, C.-C.Y., T.-L.T., B.-W.W. and S.-K.Y.; Supervision, C.-C.Y. and S.-K.Y.; Project Administration, S.-K.Y.; Funding Acquisition, M.-H.T. and S.-K.Y. All authors have read and agreed to the published version of the manuscript.

Funding: This research was funded by the Ministry of Science and Technology (MOST) under Contract No. Most 109-2221-E-005-039, 110-2221-E-005-021, 110-2811-E-005-510-MY3 and High Entropy Materials Center from The Featured Areas Research Center Program within the framework of the Higher Education Sprout Project by the Ministry of Education (MOE) under Contract No. 110QR001J4, Taiwan.

Institutional Review Board Statement: There is no Institutional Review Board relevant to our study or ethical approval required since no animal or human tests are carried out in this report.

Informed Consent Statement: Not applicable.

Data Availability Statement: Not applicable.

Acknowledgments: The authors are grateful for the support of this research by the Ministry of Science and Technology (MOST) and High Entropy Materials Center from The Featured Areas Research Center Program within the framework of the Higher Education Sprout Project by the Ministry of Education (MOE), as well as the National Center for High-performance Computing (NCHC) of

National Applied Research Laboratories (NARLabs) in Taiwan for providing computational and storage resources.

Conflicts of Interest: The authors declare no conflict of interest.

References

1. Yeh, J.-W.; Chen, S.K.; Lin, S.-J.; Gan, J.-Y.; Chin, T.-S.; Shun, T.-T.; Tsau, C.-H.; Chang, S.-Y. Nanostructured High-Entropy Alloys with Multiple Principal Elements: Novel Alloy Design Concepts and Outcomes. *Adv. Eng. Mater.* **2004**, *6*, 299–303. [[CrossRef](#)]
2. Cantor, B.; Chang, I.T.H.; Knight, P.; Vincent, A.J.B. Microstructural development in equiatomic multicomponent alloys. *Mater. Sci. Eng. A* **2004**, *375–377*, 213–218. [[CrossRef](#)]
3. Zhang, Y.; Zuo, T.T.; Tang, Z.; Gao, M.C.; Dahmen, K.A.; Liaw, P.K.; Lu, Z.P. Microstructures and properties of high-entropy alloys. *Prog. Mater. Sci.* **2014**, *61*, 1–93. [[CrossRef](#)]
4. Gao, M.C. Chapter 11: Design of High-Entropy Alloys. In *High-Entropy Alloys: Fundamentals and Applications*; Gao, M.C., Yeh, J.-W., Liaw, P.K., Zhang, Y., Eds.; Springer International Publishing: Cham, Switzerland, 2016.
5. Gao, M.C.; Zhang, B.; Guo, S.M.; Qiao, J.W.; Hawk, J.A. High-Entropy Alloys in Hexagonal Close-Packed Structure. *Metall. Mater. Trans. A* **2016**, *47*, 3322–3332. [[CrossRef](#)]
6. Senkov, O.N.; Senkova, S.V.; Woodward, C. Effect of aluminum on the microstructure and properties of two refractory high-entropy alloys. *Acta Mater.* **2014**, *68*, 214–228. [[CrossRef](#)]
7. Zhang, Z.; Mao, M.M.; Wang, J.; Gludovatz, B.; Zhang, Z.; Mao, S.X.; George, E.; Yu, Q.; Ritchie, R.O. Nanoscale origins of the damage tolerance of the high-entropy alloy CrMnFeCoNi. *Nat. Commun.* **2015**, *6*, 10143. [[CrossRef](#)]
8. Hemphill, M.; Yuan, T.; Wang, G.; Yeh, J.; Tsai, C.; Chuang, A.; Liaw, P. Fatigue behavior of Al_{0.5}CoCrCuFeNi high entropy alloys. *Acta Mater.* **2012**, *60*, 5723–5734. [[CrossRef](#)]
9. Wang, W.-R.; Wang, W.-L.; Yeh, J.-W. Phases, microstructure and mechanical properties of Al_xCoCrFeNi high-entropy alloys at elevated temperatures. *J. Alloys Compd.* **2014**, *589*, 143–152. [[CrossRef](#)]
10. Zhang, Y.; Zuo, T.; Cheng, Y.; Liaw, P.K. High-entropy Alloys with High Saturation Magnetization, Electrical Resistivity and Malleability. *Surf. Sci. Rep.* **2013**, *3*, 1455. [[CrossRef](#)]
11. Chuang, M.-H.; Tsai, M.-H.; Wang, W.-R.; Lin, S.-J.; Yeh, J.-W. Microstructure and wear behavior of Al_xCo_{1.5}CrFeNi_{1.5}Ti_y high-entropy alloys. *Acta Mater.* **2011**, *59*, 6308–6317. [[CrossRef](#)]
12. King, P.F.; Uhlig, H.H. Passivity in the iron-chromium binary alloys. *J. Phys. Chem.* **1959**, *63*, 2026–2032. [[CrossRef](#)]
13. Aronowitz, G.; Hackerman, N. The Passivity of Iron-Chromium Alloys. *J. Electrochem. Soc.* **1963**, *110*, 633. [[CrossRef](#)]
14. McBee, C.; Kruger, J. Nature of passive films on iron-chromium alloys. *Electrochim. Acta* **1972**, *17*, 1337–1341. [[CrossRef](#)]
15. Holliday, J.E.; Frankenthal, R.P. Characterization of Passivating Films on Fe-Cr Alloys by Soft X-Ray Spectroscopy. *J. Electrochem. Soc.* **1972**, *119*, 1190. [[CrossRef](#)]
16. Asami, K.; Hashimoto, K.; Shimodaira, S. An ESCA study of the Fe₂⁺/Fe₃⁺ ratio in passive films on iron-chromium alloys. *Corros. Sci.* **1976**, *16*, 387–391. [[CrossRef](#)]
17. Asami, K.; Hashimoto, K.; Shimodaira, S. Changes in the surface compositions of FeCr alloys caused by heating in a high vacuum. *Corros. Sci.* **1978**, *18*, 125–137. [[CrossRef](#)]
18. Leygraf, C.; Hultquist, G.; Olefjord, I.; Elfström, B.-O.; Knyazheva, V.; Plaskeyev, A.; Kolotykin, Y. Selective dissolution and surface enrichment of alloy components of passivated Fe₁₈Cr and Fe₁₈Cr₃Mo single crystals. *Corros. Sci.* **1979**, *19*, 343–357. [[CrossRef](#)]
19. Ogawa, H.; Omata, H.; Itoh, I.; Okada, H. Auger Electron Spectroscopic and Electrochemical Analysis of the Effect of Alloying Elements on the Passivation Behavior of Stainless Steels. *Corrosion* **2013**, *34*, 52–60. [[CrossRef](#)]
20. Sugimoto, K.; Matsuda, S. Passive and transpassive films on Fe-Cr alloys in acid and neutral solutions. *Mater. Sci. Eng.* **1980**, *42*, 181–189. [[CrossRef](#)]
21. Revesz, A.G.; Kruger, J. Passivity of metals. In *Corrosion Monographs Series*; Frankenthal, R.P., Kruger, J., Eds.; The Electrochemical Society: Pennington, NJ, USA, 1978; p. 131.
22. Hamada, E.; Yamada, K.; Nagoshi, M.; Makiishi, N.; Sato, K.; Ishii, T.; Fukuda, K.; Ishikawa, S.; Ujio, T. Direct imaging of native passive film on stainless steel by aberration corrected STEM. *Corros. Sci.* **2010**, *52*, 3851–3854. [[CrossRef](#)]
23. Marcus, P.; Maurice, V. Atomic level characterization in corrosion studies. *Philos. Trans. A Math. Phys. Eng. Sci.* **2017**, *375*, 20160414. [[CrossRef](#)] [[PubMed](#)]
24. Muangtong, P.; Rodchanarowan, A.; Chaysuwan, D.; Chanlek, N.; Goodall, R. The corrosion behaviour of CoCrFeNi-x (x = Cu, Al, Sn) high entropy alloy systems in chloride solution. *Corros. Sci.* **2020**, *172*, 108740. [[CrossRef](#)]
25. Zhang, M.; Zhang, L.; Liaw, P.K.; Li, G.; Liu, R. Effect of Nb content on thermal stability, mechanical and corrosion behaviors of hypoeutectic CoCrFeNiNb_x high-entropy alloys. *J. Mater. Res.* **2018**, *33*, 3276–3286. [[CrossRef](#)]
26. Shang, X.-L.; Wang, Z.-J.; Wu, Q.-F.; Wang, J.-C.; Li, J.-J.; Yu, J.-K. Effect of Mo Addition on Corrosion Behavior of High-Entropy Alloys CoCrFeNiMox in Aqueous Environments. *Acta Metall. Sin. Engl.* **2019**, *32*, 41–51. [[CrossRef](#)]
27. Kao, Y.-F.; Lee, T.-D.; Chen, S.-K.; Chang, Y.-S. Electrochemical passive properties of Al_xCoCrFeNi (x = 0, 0.25, 0.50, 1.00) alloys in sulfuric acids. *Corros. Sci.* **2010**, *52*, 1026–1034. [[CrossRef](#)]

28. Yen, C.-C.; Lu, H.-N.; Tsai, M.-H.; Wu, B.-W.; Lo, Y.-C.; Wang, C.-C.; Chang, S.-Y.; Yen, S.-K. Corrosion mechanism of annealed equiatomic AlCoCrFeNi tri-phase high-entropy alloy in 0.5 M H₂SO₄ aerated aqueous solution. *Corros. Sci.* **2019**, *157*, 462–471. [[CrossRef](#)]
29. Luo, H.; Li, Z.; Mingers, A.M.; Raabe, D. Corrosion behavior of an equiatomic CoCrFeMnNi high-entropy alloy compared with 304 stainless steel in sulfuric acid solution. *Corros. Sci.* **2018**, *134*, 131–139. [[CrossRef](#)]
30. Yang, H.; Shang, X.; Wang, L.; Wang, Z.; Wang, J.; Lin, X. Effect of Constituent Elements on the Corrosion Resistance of Single-Phase CoCrFeNi High-Entropy Alloys in NaCl Solution. *Acta Metall. Sin. Engl.* **2018**, *54*, 905–910. [[CrossRef](#)]
31. Gong, P.; Wang, D.; Zhang, C.; Wang, Y.; Jamili-Shirvan, Z.; Yao, K.; Wang, X. Corrosion behavior of TiZrHfBeCu(Ni) high-entropy bulk metallic glasses in 3.5 wt.% NaCl. *npj Mater. Degrad.* **2022**, *6*, 77. [[CrossRef](#)]
32. Xing, B.; Ding, Q.; Jin, B.; Zuo, X.; Zhang, N.; Yin, S. Corrosion Resistance and Passivation Behavior of CoCrFeNi-TiAl High-Entropy Alloy Coatings in Acidic Solutions. *J. Therm. Spray Technol.* **2022**, *31*, 1673–1682. [[CrossRef](#)]
33. Obot, I.; Macdonald, D.; Gasem, Z. Density functional theory (DFT) as a powerful tool for designing new organic corrosion inhibitors. Part 1: An overview. *Corros. Sci.* **2015**, *99*, 1–30. [[CrossRef](#)]
34. Nie, J.; Ao, L.; Zu, X.; Gao, H. First-principles study of O₂ adsorption on the α -U (001) surface. *J. Phys. Chem. Solids* **2014**, *75*, 130–135. [[CrossRef](#)]
35. Baseggio, O.; Romeo, M.; Fronzoni, G.; Stener, M. The near-edge X-ray-absorption fine-structure of O₂ chemisorbed on Ag (110) surface studied by density functional theory. *Surf. Sci.* **2013**, *616*, 178–185. [[CrossRef](#)]
36. Ritchie, R.O. The conflicts between strength and toughness. *Nat. Mater.* **2011**, *10*, 817–822. [[CrossRef](#)]
37. van de Walle, A.; Tiwary, P.; de Jong, M.; Olmsted, D.; Asta, M.; Dick, A.; Shin, D.; Wang, Y.; Chen, L.-Q.; Liu, Z.-K. Efficient stochastic generation of special quasirandom structures. *Calphad* **2013**, *42*, 13–18. [[CrossRef](#)]
38. Kresse, G.; Hafner, J. Ab initio molecular dynamics for liquid metals. *Phys. Rev. B* **1993**, *47*, 558–561. [[CrossRef](#)]
39. Kresse, G.; Furthmüller, J. Efficient iterative schemes for ab initio total-energy calculations using a plane-wave basis set. *Phys. Rev. B* **1996**, *54*, 11169–11186. [[CrossRef](#)]
40. Kresse, G.; Joubert, D. From ultrasoft pseudopotentials to the projector augmented-wave method. *Phys. Rev. B* **1999**, *59*, 1758–1775. [[CrossRef](#)]
41. Blöchl, P.E. Projector augmented-wave method. *Phys. Rev. B* **1994**, *50*, 17953–17979. [[CrossRef](#)]
42. Perdew, J.P.; Burke, K.; Ernzerhof, M. Generalized Gradient Approximation Made Simple. *Phys. Rev. Lett.* **1996**, *77*, 3865–3868. [[CrossRef](#)]
43. Monkhorst, H.J.; Pack, J.D. Special points for Brillouin-zone integrations. *Phys. Rev. B* **1976**, *13*, 5188–5192. [[CrossRef](#)]
44. Sillen, L.G.; Martell, A.E. *Stability Constants of Metal-Ion Complexes*; Special Publ. No. 17; Lange’s Handbook; The Chemical Society: London, UK, 1964; pp. 8–11.
45. Chen, Y.Y.; Hong, U.T.; Shih, H.C.; Yeh, J.W.; Duval, T. Electrochemical kinetics of the high entropy alloys in aqueous environments—A comparison with type 304 stainless steel. *Corros. Sci.* **2005**, *47*, 2679–2699. [[CrossRef](#)]
46. Pourbaix, M. *Atlas of Electrochemical Equilibria in Aqueous Solution*; Pergamon Press: London, UK, 1974; pp. 256–461.